Volume 16
Number 6
14 February 2020
Pages 1379–1704

Soft Matter

rsc.li/soft-matter-journal

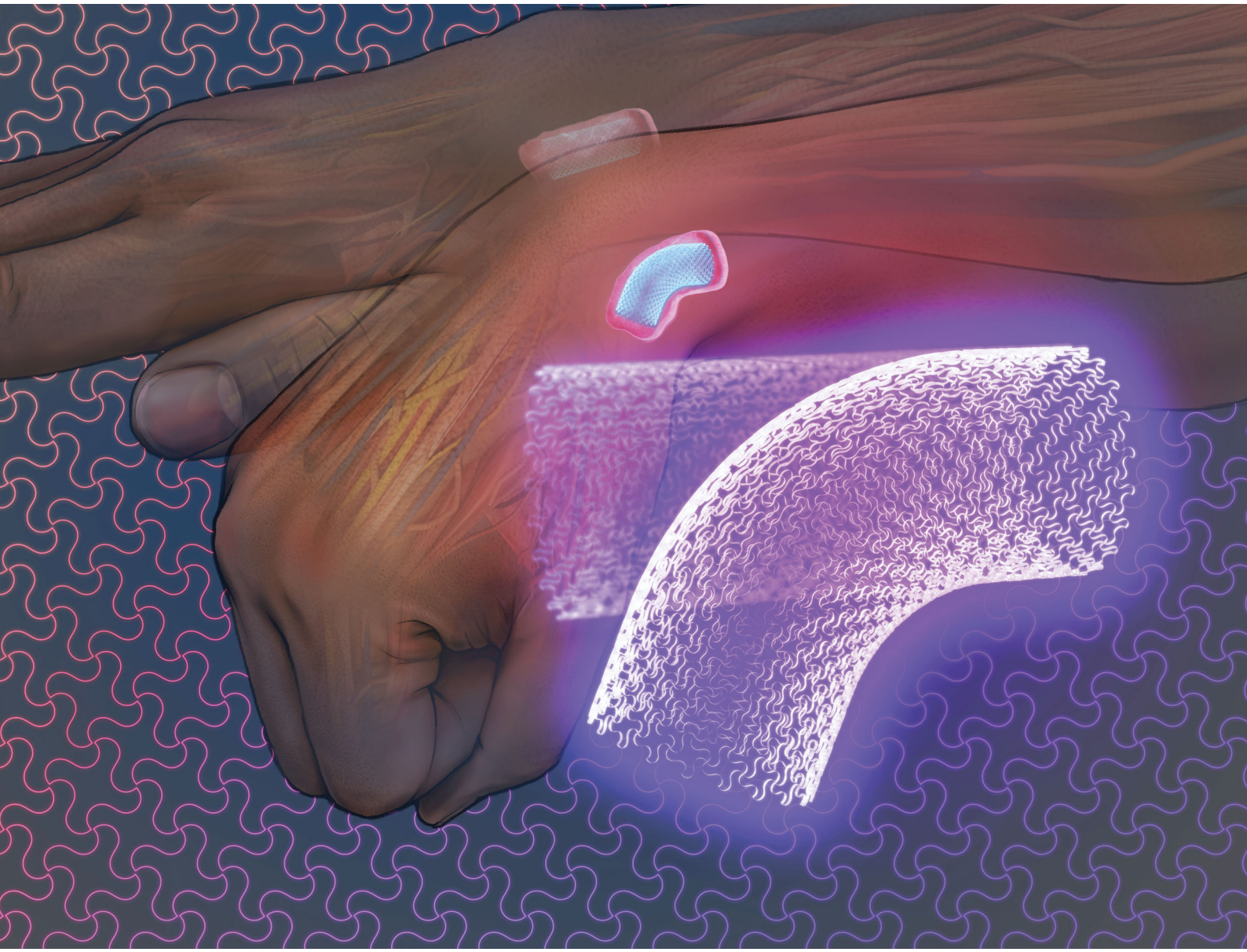

ISSN 1744-6848

ROYAL SOCIETY OF CHEMISTRY

PAPER

Dong Wang, Qi Ge *et al.*
Design framework for mechanically tunable soft biomaterial composites enhanced by modified horseshoe lattice structures

Soft Matter

PAPER

View Article Online
View Journal | View Issue

Cite this: *Soft Matter*, 2020, **16**, 1473

Design framework for mechanically tunable soft biomaterial composites enhanced by modified horseshoe lattice structures†

Dong Wang, *[ab] Yi Xiong, [b] Biao Zhang, [bc] Yuan-Fang Zhang, [b] David Rosen[bd] and Qi Ge *[be]

Soft biomaterials have a wide range of applications in many areas. However, one material can only cover a specific range of mechanical performance such as the elastic modulus and stretchability. In order to improve the mechanical performance of soft biomaterials, lattice structures are embedded to reinforce the biomaterials. In this paper, rectangular and triangular lattice structures formed by modified horseshoe microstructures are used because their mechanical properties are tunable and can be tailored precisely to match the desired properties by adjusting four geometrical parameters, the length L, radius R, width w and arc angle θ_0. A theoretical design framework for the modified horseshoe lattice structures is developed to predict the dependence of the mechanical behaviors on geometrical parameters. Both experiments and finite element simulations on lattice structures are conducted to validate the theoretical models. Results show that a wide range of design space for the elastic modulus (a few kPa to hundreds of MPa), stretchability (strain up to 180%) and Poisson ratio (ranging from −0.5 to 1.2) can be achieved. Experiments on lattice–hydrogel composites are also conducted to verify the reinforcement effect of lattice structures on the hydrogel. This work provides a theoretical method to predict the mechanical behaviors of the lattice structures and aid the rational design of reinforced biomaterials, which has applications in tissue engineering, drug delivery and intraocular lenses.

Received 25th October 2019,
Accepted 6th January 2020

DOI: 10.1039/c9sm02119a

rsc.li/soft-matter-journal

1 Introduction

Soft biomaterials are the soft materials interacting with biological systems to evaluate, treat, augment or replace any tissue, organ or function of the body.[1] The wide applications of soft biomaterials can be found in the fields of artificial tissues,[2,3] drug delivery,[4,5] vascular grafts,[6,7] intraocular lenses,[8] stents[9] and many others.[10–12] The commonly used soft biomaterials include polystyrene, poly(L-lactic acid) (PLLA), poly(lactic acid) (PLA) and poly(lactic-*co*-glycolic acid) (PLGA) for porous scaffolds to culture cells in tissue engineering,[13–16] polymethyl methacrylate (PMMA) for intraocular lenses,[8] poly(dimethylsiloxane) (PDMS) for drug delivery vehicles and blood-contacting biomaterials,[17] and synthetic hydrogels such as poly(ethylene glycol)diacrylate (PEGDA) for drug delivery and tissue engineering.[18,19] However, one material can only cover a specific range of mechanical properties such as elastic modulus and stretchability. For example, the unique structural similarity with biological extracellular matrices and excellent biocompatibility make hydrogels the leading candidate for tissue engineering scaffolds. However, the low elastic modulus of hydrogels constrains them from other applications.[20–22] Although the elastic modulus of hydrogels can be somewhat increased by increasing the cross-linking density, this approach generally sacrifices its biological properties and stretchability.[8,23,24]

In contrast, natural biological tissues cover a wide range of mechanical properties, as indicated in Fig. 1. For example, gastrointestinal tract can be stretched by over 1.5 times its initial shape with a modulus up to 0.8 MPa, which is difficult achieve with a single soft synthetic material. Inspired by the architecture of the native tissue whose unique mechanical properties are derived from a fibrous protein framework that supports the soft matrix, researchers have proposed approaches to enhance the stiffness of synthetic soft biomaterials by

[a] *Robotics Institute, School of Mechanical Engineering, Shanghai Jiao Tong University, Shanghai 200240, China. E-mail: wang_dong@sjtu.edu.cn*
[b] *Digital Manufacturing and Design Centre, Singapore University of Technology and Design, Singapore 487372, Singapore*
[c] *Xi'an Institute of Flexible Electronics and Xi'an Key Laboratory of Biomedical Materials & Engineering, Northwestern Polytechnical University (NPU), Xi'an 710072, Shaanxi, China*
[d] *The George W. Woodruff School of Mechanical Engineering, Georgia Institute of Technology, 813 Ferst Drive, NW, Atlanta, GA 30332-0405, USA*
[e] *Department of Mechanical and Energy Engineering, Southern University of Science and Technology, Shenzhen 518055, China. E-mail: geq@sustech.edu.cn*

† Electronic supplementary information (ESI) available. See DOI: 10.1039/c9sm02119a

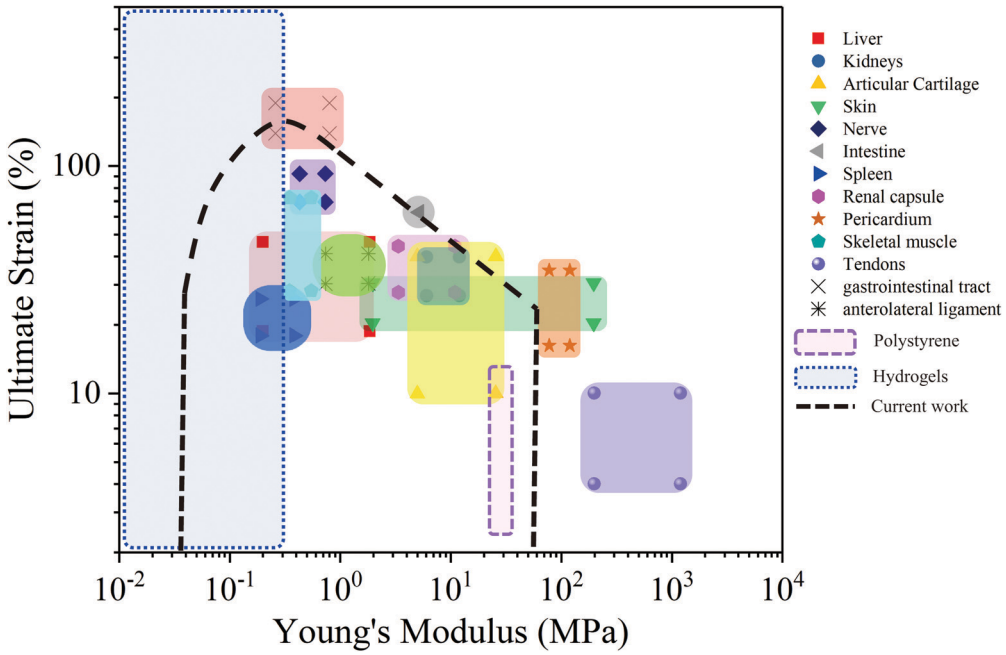

Fig. 1 Young's moduli and ultimate strains of soft natural and synthetic biomaterials: liver,[25] kidneys,[25] articular cartilage,[26] skin,[27–29] nerve,[30] intestine,[31] spleen,[32,33] renal capsule,[33] pericardium,[34] skeletal muscle,[35] tendons,[36,37] gastrointestinal tract,[38] anterolateral ligament,[39] polystyrene,[40] and hydrogels.[41,42] The black dashed curves show the schematics of the design space of this work.

embedding reinforced structures made of stiff materials. For example, a fiber-reinforced composite with increased modulus was fabricated by embedding adjustable collagen fibers within a protein matrix;[43] a biohybrid composite with high flexibility and strength was fabricated by aligning elastomeric fibers into an extracellular matrix gel.[44] However, the lower failure strains of these stiff materials significantly limit the deformability of the reinforced synthetic biomaterials. In order to resolve the failure strain mismatch between the stiff reinforcing materials and the soft matrix, Jang *et al.*[29] developed bio-inspired, soft deterministic composites that were realized by embedding a uniform lattice structure consisting of repeating, filamentary building block units with 'horseshoe' geometries into a low-modulus supporting matrix. The 'horseshoe' building block was formed by anti-symmetrically connecting two identical circular arcs, and the composites can yield a wide range of desired mechanical properties including isotropic/anisotropic responses and spatially heterogeneous characteristics by tuning the arc angle, radius and width of the circular arcs.[29,45] However, this design method is mainly used in the design of flexible electronics, and the ultimate strains in most of the demonstrated examples are less than 60%. In addition, some biological tissues such as arterial endothelium[46] and membranes[47] exhibit negative Poisson ratios, *i.e.*, the transverse direction expands as they are stretched in the longitudinal direction. In order to match this unusual behavior of these biological tissues, synthetic soft materials with negative Poisson ratios are desired.

In this paper, we report a design framework for soft biomaterial composites that are reinforced by stiff and stretchable rectangular/triangular lattice structures (Fig. 2a and b) constructed by repeating modified horseshoe microstructures. Fig. 2c depicts

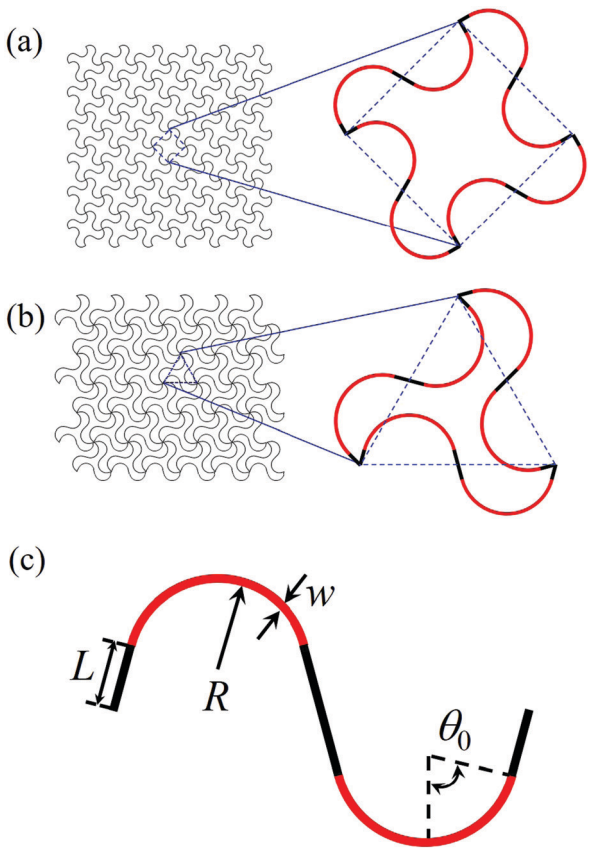

Fig. 2 Schematic illustration of (a) rectangular (upper) and (b) triangular (lower) modified horseshoe lattices with their representative units; (c) a single modified horseshoe structure.

the details of the modified horseshoe microstructure where two identical circular arcs are arranged anti-symmetrically and connected with two straight beams. Each circular arc has a radius of R and an arc angle of $2\theta_0$ and the length of each straight beam is L. The width of the entire microstructure is w. Different from the horseshoe microstructure used in Jang's work,[29] we add the straight beams to introduce an additional design freedom and further increase the stretchability of the stiff lattice structures. The mechanical properties of the reinforced biomaterial composite lattice structures, such as modulus, stretchability and Poisson ratio, are highly tunable by changing the four key design parameters, R, w, L and θ_0. As highlighted in Fig. 1, soft biomaterial composites designed by our approach can exhibit moduli from a few kPa to hundreds of MPa and stretchability up to 180% depending on the choices of design parameters. Experiments are conducted to validate the design framework.

2 Theoretical derivation

In order to interpret the elastic behaviors of a single modified horseshoe microstructure and the lattice structures formed with the modified horseshoe microstructures, and aid the design of lattice structure-reinforced biomaterial composites, a theoretical model for the lattice structure is developed. The theoretical model is based on the work of Ma *et al.*,[45] where the length L of the straight beam shown in Fig. 2(c) is zero. We develop the theory to a more general case in which the effect of L is incorporated. The straight beams are assumed to be straight during stretching. The assumption is made based on the fact that most of the deformation occurs on the circular arcs of the horseshoe repeating units and it is verified by finite element simulations and experiments in Section 3. The model of a single modified horseshoe structure is developed first, and the modified horseshoe lattice structure is modeled next. For simplicity, we set $\theta_0 = \pi/2$ in the following derivation. Nevertheless, this approach can be generalized to study the elastic behaviors of the lattice structure with other values of θ_0.

2.1 Theoretical derivation of a single horseshoe structure

As schematically depicted in Fig. 3(a), when a hierarchical lattice structure is subjected to a uniaxial stretching, each horseshoe microstructure undergoes anti-symmetric deformation with respect to the central point (the red dot in Fig. 3(a)) due to the periodicity of the lattice structures. Based on the previous study,[45] we consider that the modified horseshoe microstructure is simply supported (Fig. 3(a)). A force F_x along the central line and a force F_y along the vertical direction are applied at each end of the microstructure, and a pair of moments M_0 are anti-symmetrically located at the two ends of the microstructure. The geometric anti-symmetricity allows us to take half of the modified horseshoe microstructure to perform the analysis. As shown in Fig. 3(b) and (c), the undeformed and deformed right half of the modified horseshoe microstructure was analysed.

Fig. 3(d) and (e) describe an infinitesimal curved segment of the modified half horseshoe microstructure in the undeformed and deformed configurations, which are represented by the X–Y and x–y coordinates, respectively. In the undeformed configuration, the angle α between the centroid axis and horizontal line is in the range of $[-\alpha_0,\alpha_0]$, where the positive (or negative) sign represents a counterclockwise (or clockwise) rotation from the X axis to the tangential direction of the segment. In the deformed configuration, the corresponding angle θ is in the

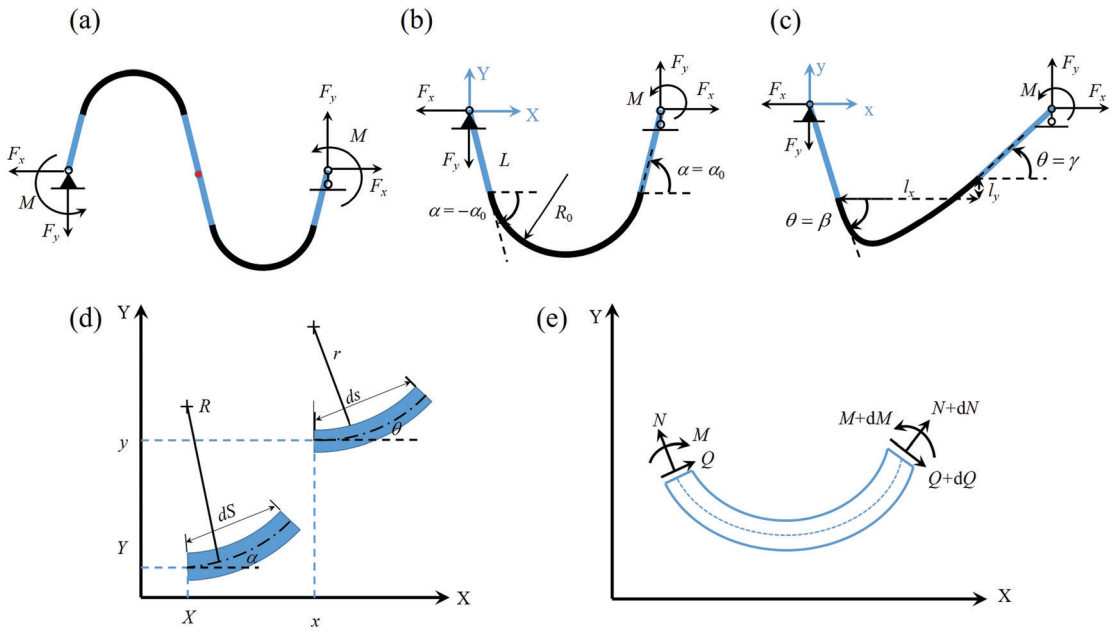

Fig. 3 (a) Schematics of a modified horseshoe microstructure under an axial force F_x, a shear force F_y and a moment M_0 at two ends; (b) half of a modified horseshoe microstructure under F_x, F_y and M_0; (c) illustration of the deformed shape of half of the modified horseshoe microstructure; (d) deformation of a length element; (e) forces and moment sign conventions.

range of [β,γ]. Therefore, the rotational angle φ resulting from the deformation is θ–α. Under stretching, the length of the infinitesimal segment at the centroid axis varies from dS to ds, and the engineering strain at the centroid axis is $\varepsilon = (\mathrm{d}s - \mathrm{d}S)/\mathrm{d}S$, where $\mathrm{d}S = R\mathrm{d}\alpha$ and $\mathrm{d}s = r(\theta)\mathrm{d}\theta$. R is the radius of the arc in the modified horseshoe microstructure at the undeformed configuration, and $r(\theta)$ denotes the radius of the deformed arc, which is a function of the deformed angle θ.

Fig. 3(e) presents the axial force N, the shear force Q and the bending moment M at any cross section, and they can be calculated by

$$N = EA\varepsilon, \quad M = EI(1+\varepsilon)\frac{\mathrm{d}\varphi}{\mathrm{d}s} = EI\frac{\mathrm{d}\varphi}{\mathrm{d}S},$$

with Young's modulus E, the cross-sectional area A ($A = w \times d$) of the modified horseshoe microstructure, and the second area moment I ($I = w^3d/12$). d represents the thickness of the structure in the Z direction. The axial force N, the shear force Q and the bending moment M satisfy the following equilibrium equations:[48]

$$\frac{\mathrm{d}N}{\mathrm{d}s} + \frac{Q}{r} = 0, \quad -\frac{N}{r} + \frac{\mathrm{d}Q}{\mathrm{d}s} = 0, \quad \frac{\mathrm{d}M}{\mathrm{d}s} = Q.$$

Based on the loading condition shown in Fig. 3(c), the axial and shear forces can be calculated as:

$N = F_x\cos\theta + F_y\sin\theta$, and $Q = F_x\sin\theta - F_y\cos\theta$.

Rearranging the above equations, ε and $\mathrm{d}^2\varphi/\mathrm{d}S^2$ can be rewritten as:

$$\varepsilon = \left(F_x\cos\theta + F_y\sin\theta\right)/EA,$$

$$\frac{\mathrm{d}^2\varphi}{\mathrm{d}S^2} = \frac{(EA + F_x\cos\theta + F_y\sin\theta)(F_x\sin\theta - F_y\cos\theta)}{EI \times EA}.$$

By using $\mathrm{d}S = R\mathrm{d}\alpha$, $\mathrm{d}^2\varphi/\mathrm{d}S^2 = \frac{1}{R^2} \times \mathrm{d}^2\varphi/\mathrm{d}\alpha^2$ and $\mathrm{d}\left[\left(\frac{\mathrm{d}\theta}{\mathrm{d}\alpha}\right)^2\right] \Big/ \mathrm{d}\theta = 2\frac{\mathrm{d}^2\theta}{\mathrm{d}\alpha^2}$, the above equation can be written as

$$\mathrm{d}\left[\left(\frac{\mathrm{d}\theta}{\mathrm{d}\alpha}\right)^2\right] = 2 \times \frac{R^2(EA + F_x\cos\theta + F_y\sin\theta)(F_x\sin\theta - F_y\cos\theta)}{EI \times EA} \times \mathrm{d}\theta.$$

Conducting integration on both sides and applying the boundary conditions, $(\mathrm{d}\theta/\mathrm{d}\alpha)^2$ can be calculated as:

$$\frac{\mathrm{d}\theta}{\mathrm{d}\alpha} = f(\theta, l_x, l_y),$$

where the expression of $f(\theta,l_x,l_y)$ is given in the ESI.† l_x and l_y are the distances between the two ends of the deformed arc in the x and y directions. After rearranging the above equation, one can integrate the rearranged equation on both sides:

$$\int_{\theta=\beta}^{\theta=\gamma} \frac{\mathrm{d}\theta}{f(\theta, l_x, l_y)} = \int_{\alpha=-\alpha_0}^{\alpha=\alpha_0} \mathrm{d}\alpha. \quad (1)$$

The horizontal and vertical distances l_x and l_y can be calculated as $l_x = \int\cos\theta\mathrm{d}s$ and $l_y = \int\sin\theta\mathrm{d}s$. Recall that $\mathrm{d}s = (1+\varepsilon)\mathrm{d}S$, $\mathrm{d}S = R\mathrm{d}\alpha$, and $\mathrm{d}\alpha = \mathrm{d}\theta/f(\theta,l_x,l_y)$; therefore l_x and l_y can be computed as

$$l_x = \int_\beta^\gamma \frac{R(1+\varepsilon)\cos\theta}{f(\theta, l_x, l_y)}\mathrm{d}\theta, \quad (2)$$

and

$$l_y = \int_\beta^\gamma \frac{R(1+\varepsilon)\sin\theta}{f(\theta, l_x, l_y)}\mathrm{d}\theta. \quad (3)$$

In addition, the geometric compatibility requires:

$$L\sin\beta + L\sin\gamma + l_y = 0. \quad (4)$$

By using the four equations eqn (1)–(4), the four unknown β, γ, l_x, and l_y can be solved.

2.2 Theoretical model for the hierarchical lattice structure

A rectangular hierarchical lattice structure formed by modified horseshoe microstructures under uniaxial vertical stress σ is taken as an example to illustrate the theoretical modelling of the lattice structures. Due to the periodical arrangements of the rectangular horseshoe units, a representative unit cell was analyzed, as shown in Fig. 4. Each representative unit cell consists of four modified horseshoe microstructures, indexed from 1 to 4. The schematics of the undeformed and deformed shapes are shown in Fig. 4(b) and (c). The inner forces and moment on each modified horseshoe microstructure are denoted by F_{xi}, F_{yi} and M_i, where i = 1, 2, 3 and 4, as shown in Fig. 4(d). Due to the anti-symmetry of the representative unit around its central point, the inner force, moment and deformation of microstructures 1 and 3 are the same and those of microstructures 2 and 4 are the same. The static equilibrium of the representative unit requires that the inner force at the joint between microstructure 1 and 2 is zero in both X and Y directions, which yields:

$$F_{x1}\cos\alpha_3 - F_{y1}\sin\alpha_3 + F_{x2}\cos\alpha_1 + F_{y2}\sin\alpha_1 = 0, \quad (5)$$

$$F_{x2}\sin\alpha_1 - F_{x1}\sin\alpha_3 - F_{y1}\cos\alpha_3 - F_{y2}\cos\alpha_1 = 0. \quad (6)$$

The external loading on the representative unit is σ, thus it can be obtained that in the Y direction:

$$(F_{x1}\sin\alpha_3 + F_{y1}\cos\alpha_3) + (F_{x4}\sin\alpha_1 - F_{y4}\cos\alpha_1) = 4\sqrt{2}\sigma Rd, \quad (7)$$

and in the X direction:

$$(-F_{x1}\cos\alpha_3 + F_{y1}\sin\alpha_3) + (F_{x4}\cos\alpha_1 - F_{y4}\sin\alpha_1) = 0. \quad (8)$$

The moment equilibrium of an arbitrary joint, which is connected by 4 modified horseshoe microstructures, requires that

$$\sum_{i=1}^{4} M_i = -\sum_{i=1}^{4}(F_{yi}L_i)/2 = 0, \quad (9)$$

where $L_i = 2(L\cos\beta + l_{xi} + L\cos\gamma)$($i$ = 1, 2, 3, or 4) is the distance between two ends of the modified horseshoe microstructure in

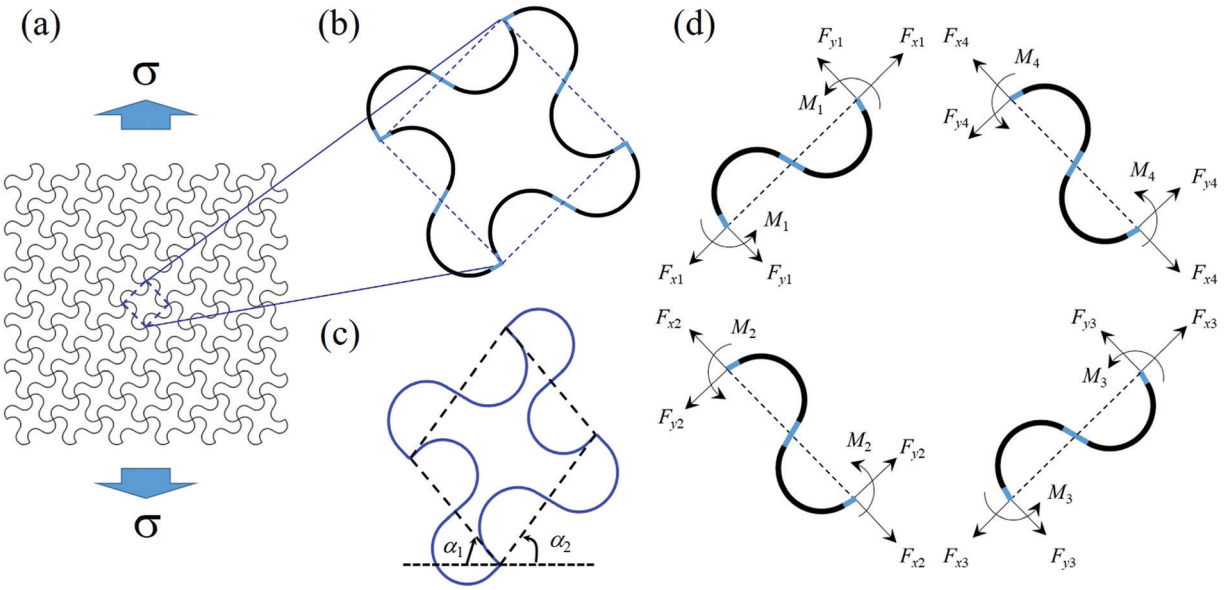

Fig. 4 (a) Schematics of a rectangular modified horseshoe lattice structure under uniaxial vertical stress σ. Undeformed (b) and deformed (c) shapes of a representative unit. (d) Inner forces and moment for each modified horseshoe microstructure in the representative unit.

the deformed configuration. The angle between the tangent directions of two connected horseshoe microstructures remains unchanged during deformation, thus we have

$$\theta_0 = \alpha_1 + \alpha_2 + \gamma_1 - \gamma_2, \tag{10}$$

where α_1 and α_2 are shown in Fig. 4(c). For the horseshoe microstructures 1 and 2, we have

$$\int_{\beta_i}^{\gamma_i} \frac{1}{f_i(\theta, l_x, l_y)} \mathrm{d}\theta = \int_{-\alpha_0}^{\alpha_0} \mathrm{d}\alpha, \tag{11}$$

$$\int_{\beta_i}^{\gamma_i} \frac{R(1+\varepsilon_i)\cos\theta}{f_i(\theta, l_x, l_y)} \mathrm{d}\theta = l_x, \tag{12}$$

$$\int_{\beta_i}^{\gamma_i} \frac{R(1+\varepsilon_i)\sin\theta}{f_i(\theta, l_x, l_y)} \mathrm{d}\theta = l_y, \tag{13}$$

$$L_i \sin\beta_i + L_i \sin\gamma_i + l_{yi} = 0, \tag{14}$$

where $i = 1$ or 2, and β_i is the angle at the beginning of the the horseshoe microstructure i. By using $F_{x3} = F_{x1}$, $F_{x4} = F_{x2}$, $F_{y3} = F_{y1}$ and $F_{y4} = F_{y2}$, and solving the 14 equations eqn (5)–(14), the 14 unknowns F_{x1}, F_{x2}, F_{y1}, F_{y2}, β_1, β_2, γ_1, γ_2, l_{x1}, l_{x2}, l_{y1}, l_{y2}, α_1 and α_2 can be solved. The deformation of a triangular hierarchical lattice structure under uniaxial stress can be solved in a similar way and the details of the solution are not shown here.

3 Validation of the theoretical model

In this section, the fabrication procedures of the lattice structures and lattice–hydrogel composites are introduced. Experiments on both rectangular and triangular lattice structures are then conducted to validate the theoretical framework.

3.1 Fabrication procedures

Both the rectangular and triangular lattice structures are printed using a commercial Polyjet multimaterial 3D printer (Stratasys, Connex 500). VeroCyan is chosen as the material, as it is easy to use to print the lattice structure with high resolution using the commercial printer. The lattice–hydrogel composite is made by infusing the pre-gel solution into the printed lattice structure and then curing it under UV light. The hydrogel is based on acrylamide–PEGDA and can be stretched by more than 1300%.[49] Detailed procedures are shown below. A hydrogel precursor is prepared by mixing acrylamide (Sigma Aldrich) as monomer, PEGDA (Sigma Aldrich) as the crosslinker, and self-developed highly water-soluble 2,4,6-trimethylbenzoyldiphenylphosphine oxide (TPO) nanoparticles as the photoinitiator in water. The solution consists of 80 wt% water, 20% acrylamide–PEGDA mixture with the PEGDA (700)/acrylamide mixing ratio of 0.625 wt%, and 0.5 wt% TPO nanoparticles. TPO-based nanoparticles were prepared according to a previously published protocol.[50] TPO-based nanoparticles were first added into deionised water, and the mixture was stirred by a magnetic stirrer for 10 minutes. Acrylamide was then added into the mixture and it was stirred for 5 minutes until it had completely dissolved. PEGDA was added next. The pre-gel solution was then infused into the printed lattice structure and the composite was cured by a near UV light (405 nm) for 8 minutes.

3.2 Model verification

The comparisons between experimental and theoretical results of the rectangular lattice structure under uniaxial tensile loading are shown in Fig. 5. The loading rate is 0.3 mm s^{-1}, which is slow to reduce the viscosity effect of the material. The experimental (blue), theoretical (yellow) and FE simulation (black) results agree well. The uniaxial tensile test results of the hydrogel and

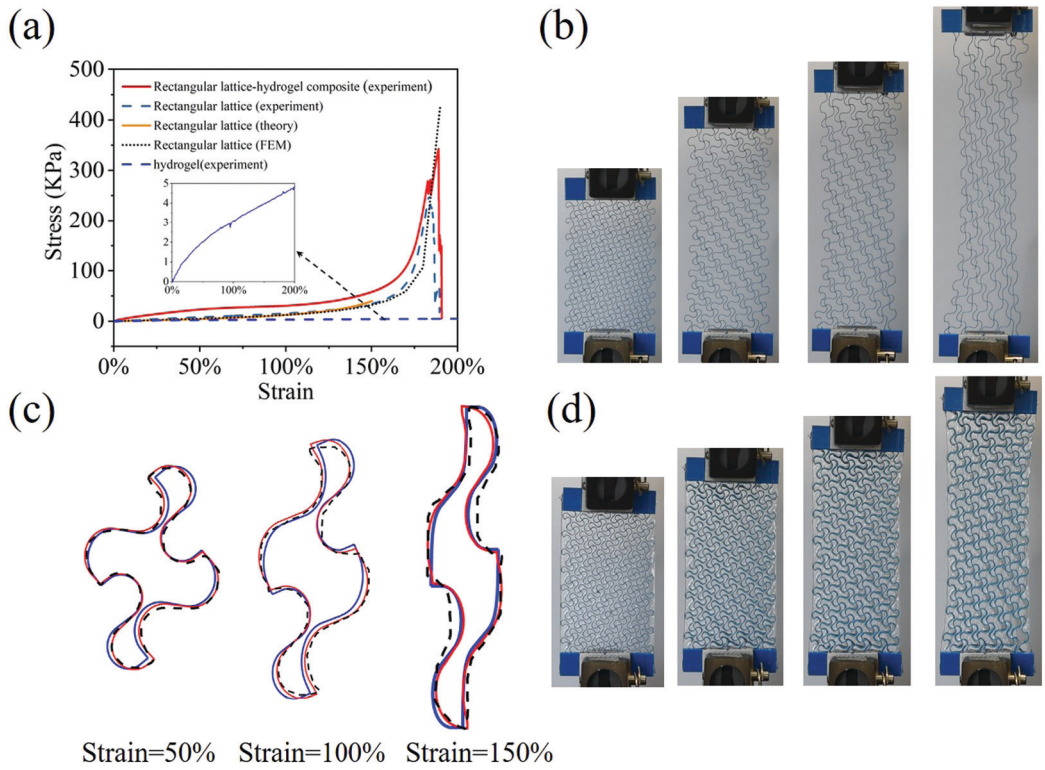

Fig. 5 (a) Experimental, theoretical and FE stress–strain curves for a rectangular modified horseshoe lattice. The experimental stress–strain curves of a rectangular lattice–hydrogel composite and hydrogel are shown. The inset shows the data for the hydrogel. (b) Snapshots of the lattice at different strains. (c) Comparison between experimental (black dashed), theoretical (blue solid) and FE simulation (red solid) deformed shapes of a representative unit at different strains. (d) Snapshots of the lattice–hydrogel composite at different strains.

lattice–hydrogel composite are also shown in Fig. 5(a) for comparison. Both the lattice structure and lattice–hydrogel composite exhibit nonlinear J-shaped stress–strain curves, which show an ultralow effective modulus at the ''toe'' region induced by the bending of the arc part of the horseshoe microstructure, an increased modulus at the ''heel'' region caused by rotating, twisting and aligning of the horseshoe microstructure to the direction of the applied stress and a large modulus at the ''linear'' region induced by the stretching of the filaments. The failure strains of both the lattice structure and lattice–hydrogel composite are around 180%. While the failure of the lattice structure is due to the fracture of the fiber material (Fig. 5(b)), the debonding of the hydrogel and lattice structure leads to the failure of the lattice–hydrogel composite (Fig. 5(d)). Moreover, the hydrogel is significantly reinforced by the lattice structure. After reinforcement by the lattice structure, the Young's modulus of the hydrogel increases from $\sim$2 kPa to $\sim$30 kPa at the ''toe'' region and $\sim$500 kPa at the ''linear'' region.

The experimental (black dashed) deformed shapes of the rectangular lattice structures are plotted and compared with the theory (blue solid)/FEM simulation (red solid) results in Fig. 5c. The periodical unit at the center of the structure is chosen to reduce the boundary effect. The coordinate of each point of the unit is chosen using ImageJ and then processed by Matlab code. From Fig. 5c, it can be seen that all of the theoretical, experimental and FEM results agree well, even when the strain reaches 150%. The differences between the theoretical, experimental and FEM deformed shapes are less than a rotation of 5° around its center.

Experiments on the triangular lattice structure under uniaxial loading are also conducted and compared with theoretical and FEM results. As can be seen from Fig. 6(a), as the strain of the triangular lattice structure is less than 50%, the discrepancy between the experimental, theoretical and FEM stress is less than 10%. But as the strain increases, the discrepancy becomes larger. It can be observed in Fig. 6(b) that the triangular lattice structure exhibits a negative Poisson ratio. All of the theoretical (blue solid), experimental (black dashed) and FEM (red solid) deformed shapes verify this phenomenon, as shown in Fig. 6(c). For the triangular lattice–hydrogel composite, its Poisson ratio is nearly 0 because of the contraction force generated by the hydrogel as the triangular lattice expands.

In Fig. 6c, it can be observed that when the strain is smaller than 50%, theoretical, experimental and FEM deformed shapes agree well. But when the strain is 70%, there are some discrepancies between the theoretical modeling, the experiments and FEM results. This is because of the prominent boundary effect of the triangular lattice structures, which is neglected by the theoretical model. In contrast to the rectangular lattice structure, the vortex number in a unit of the triangular lattice structures is smaller and each vortex in a unit is connected through a horseshoe microstructure, thus the force can be more efficiently transferred in the triangular lattice structures.

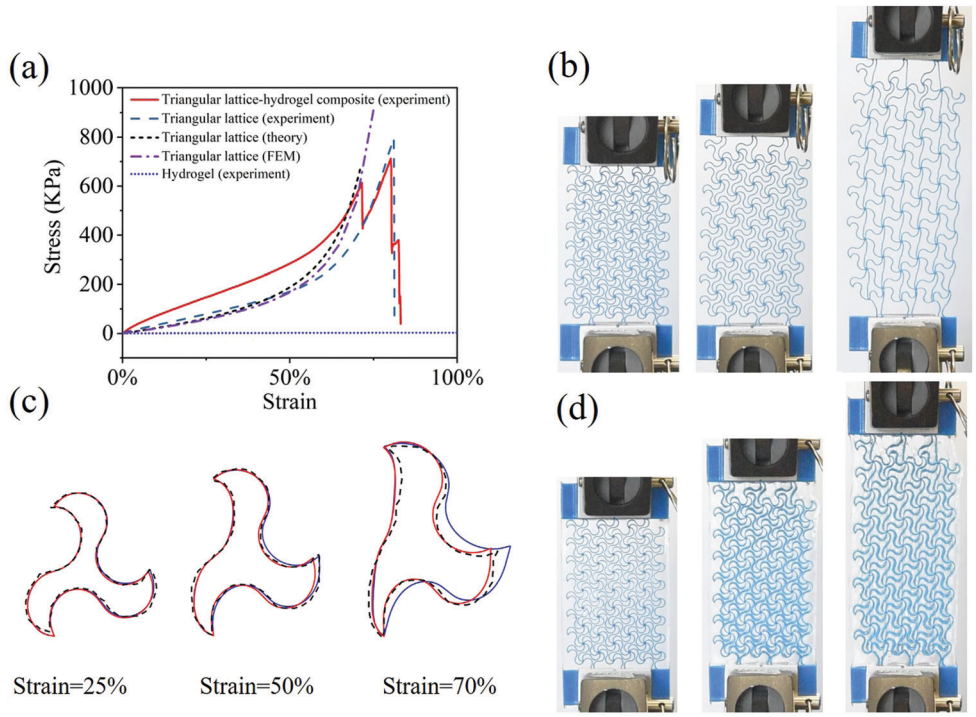

Fig. 6 (a) Experimental, theoretical and FEM stress–strain curves for a triangular modified horseshoe lattice. The experimental stress–strain relations of a triangular lattice–hydrogel composite and hydrogel are shown in red and blue dashed curves, respectively. (b) Snapshots of the lattice at different strains. (c) Experimental (black dashed), theoretical (blue solid) and FEM (red solid) deformed shapes of a representative unit at different strains. (d) Snapshots of the lattice–hydrogel composite at different strains.

Therefore, clamping force on the boundary will generate a larger effect on the units in the center for a triangular lattice structure. As shown in Fig. 6(b), a prominent boundary effect is generated in the triangular lattice structure.

The distribution of the local maximum principal strain on a rectangular horseshoe unit in the finite element simulation is shown in Fig. 7. The strain of the whole unit is 125%, while the local maximum principal strain is less than 3%. This shows that our assumption of small strain is valid, and the straight beam can be assumed to be straight after deformation.

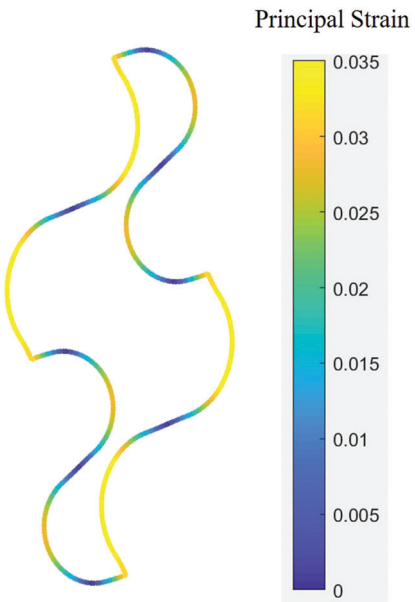

Fig. 7 The distribution of the local maximum principal strain on a representative rectangular horseshoe unit in a finite element simulation. The unit is stretched in the vertical direction with a strain of 125%.

4 Numerical results

In this section, we use the developed theoretical model to predict the mechanical behaviors of the horseshoe microstructure and lattice structures, and explore their abilities as reinforced structures in hydrogels. The effects of L/w on the modified horseshoe microstructure, and the rectangular and triangular lattice structures are presented first. Next, the effects of θ_0 on the rectangular and triangular lattice structures are studied. Unless otherwise specified, the geometrical parameters used are w = 0.133 mm, R/w = 10, d/w = 7.5, L/w = 5, and $\theta_0 = \pi/2$ and the Young's modulus of the fiber material is E = 1.2 GPa.

4.1 Effects of L

In Fig. 8(a), the relation between the applied uniaxial tensile force and the corresponding strain is plotted for samples with different L/w = 0 to 5. The undeformed (red dashed) and deformed (blue solid) curves of the modified horseshoe microstructure are shown in Fig. 8(b). It can be seen that the strain of the microstructure increases as L/w increases due to the

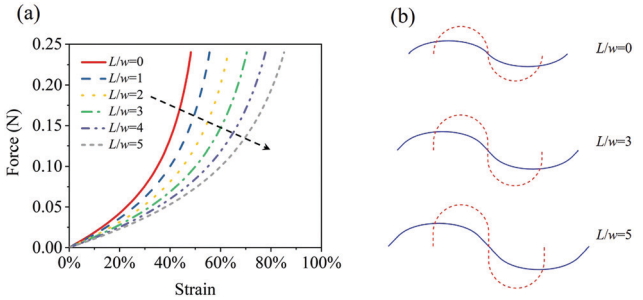

Fig. 8 (a) Force–strain curves for a modified horseshoe microstructure with different length L. (b) Deformed (blue solid) and undeformed (red dashed) shapes of the horseshoe microstructure with different length L.

rotation and alignment of the straight beam to the direction of applied force. For example, under a constant force of 0.2 N, the strains of the microstructure with $L/w = 0$ and 5 are $\sim$45% and $\sim$80%, respectively.

Similar to the modified horseshoe microstructure, the strain of the rectangular lattice structure under a vertical tensile stress also increases with increasing L/w, as shown in Fig. 9(a). The deformed and undeformed shapes of a representative unit are plotted in Fig. 9(c). It can be seen clearly that the rotation and alignment of the initially straight beams lead to the increase of the strain. The relation between the Poisson ratio and the vertical strain is shown in Fig. 9(b). With the increase of L/w, the Poisson ratio decreases.

The dependence of the applied uniaxial tensile stress and the Poisson ratio of the triangular lattice structure on strain for different L/w is shown in Fig. 10. Similarly, the strain increases with the increase of L/w. However, the Poisson ratio is negative for all triangular lattice structures with different L/w, in contrast to the rectangular lattice structures, as shown in Fig. 10(b). Its magnitude is larger for larger L/w at relatively smaller strain, indicating that the transverse direction expands more. With the increase of the strain, the magnitude of the Poisson ratio increases. The negative Poisson ratio can be seen from the theoretical deformed and undeformed shapes of the triangular lattice structures with different L/w = 0, 3 and 5 under the same vertical stress, as shown in Fig. 10(c).

4.2 Effects of θ_0

By varying θ_0, the stiffness and Poisson ratio of the rectangular lattice can change significantly. In Fig. 11(a), the theoretical predicted stress–strain curves are plotted for different angles of θ_0 = 30°, 45°, 60°, 75° and 90°. As θ_0 decreases, the structure becomes stiffer and more difficult to be deformed due to the decrease of the length of the arc part. It can be observed from Fig. 11(b) that the Poisson ratio increases as θ_0 decreases and can reach 1.2 for θ_0 = 30°, which indicates that the transverse displacement can be even larger than the longitudinal displacement, as shown in Fig. 11(c). This phenomenon can be adopted to design reinforced structures for hydrogels with unusual Poisson ratio effects.

The effect of θ_0 on the triangular lattice is similar to that of the rectangular lattice, as shown in Fig. 12. The stiffness of the triangular lattice structure increases as θ_0 decreases

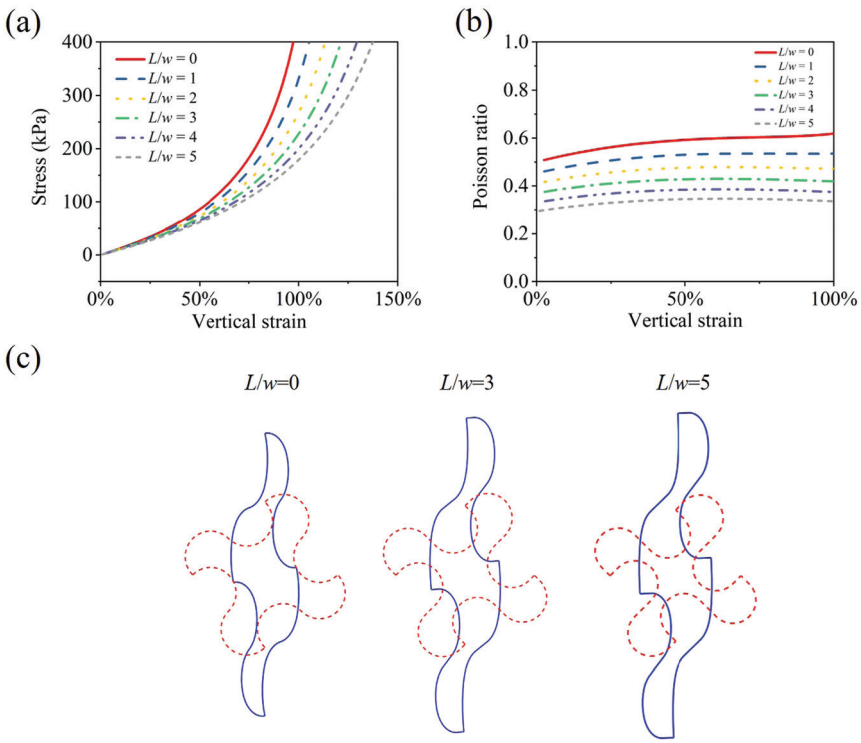

Fig. 9 (a) Stress–strain curves for a rectangular modified horseshoe lattice with different length L. (b) The dependence of Poisson ratio on strain for the lattice with different L/w. (c) Theoretical undeformed (red dashed) and deformed (blue) shapes of the lattice with different L/w.

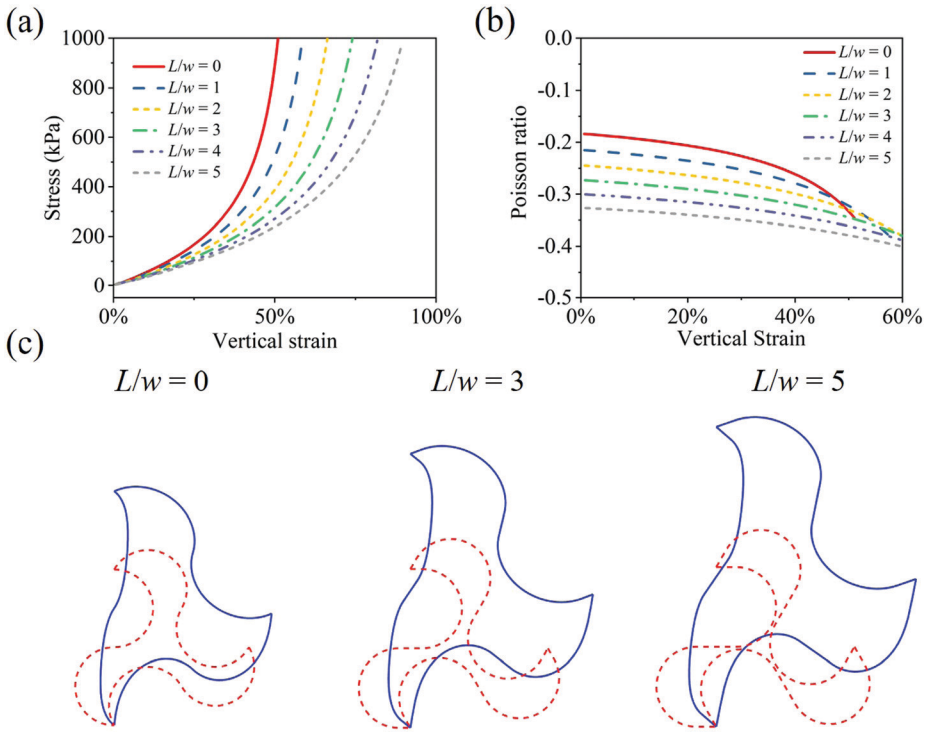

Fig. 10 (a) Stress–strain curves for a triangular modified horseshoe lattice with different length L/w. (b) The dependence of the Poisson ratio on the vertical strain for the lattice with different length L/w. (c) Theoretical undeformed (red dashed) and deformed (blue) shapes of the lattice with different L/w.

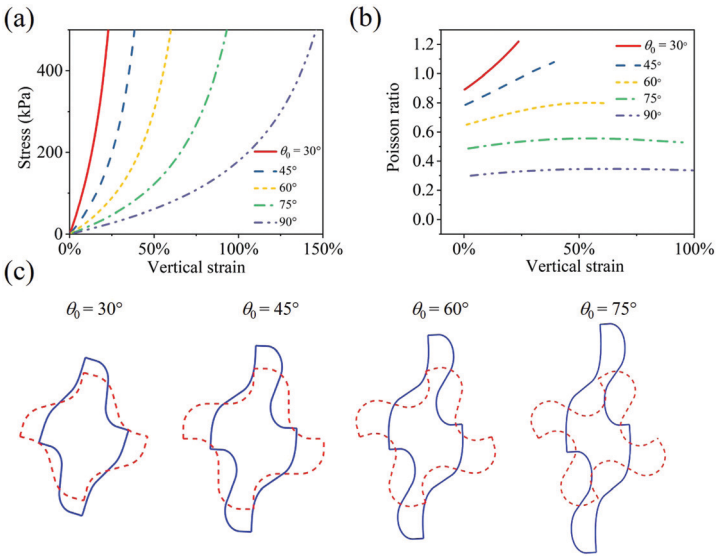

Fig. 11 (a) Stress–strain curves of a rectangular lattice under vertical tensile stress with different θ_0. (b) The dependence of the Poisson ratio on vertical strain for the rectangular lattice with different θ_0. (c) Undeformed (red dashed) and deformed (blue) shapes of the rectangular lattice with different θ_0.

from 90° to 30°. For example, under a constant vertical stress of 900 kPa, the vertical strain of triangular lattice structure with θ_0 = 30° is 2.93%, while the triangular lattice structure with θ_0 = 90° exhibits a larger vertical strain of 89.9%. The magnitude of the Poisson ratio increases with decreasing θ_0, as shown in Fig. 12(b). It can be observed that the triangular lattice structure with larger θ_0 exhibits a wider range of available combinations of vertical strain and Poisson ratio, which provides rich choices of the geometric parameters of the reinforced lattice for the hydrogel.

5 Discussion

The essential difference between the current and previous work on the reinforced lattice structure lies in the use of the modified

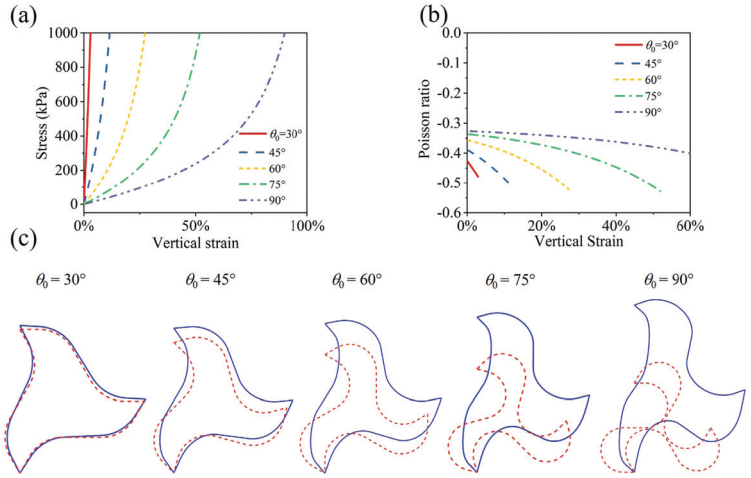

Fig. 12 (a) Stress–strain curves for a triangular lattice under vertical tensile stress with different θ_0. (b) The dependence of the Poisson ratio on vertical strain for the triangular lattice with different θ_0. (c) Undeformed (red dashed) and deformed (blue) shapes of the triangular lattice with different θ_0.

horseshoe lattice structures to match both the Young's moduli and stretchability of the soft materials. Currently, most structures that are applied to reinforce the soft biomaterials are made from stiff materials with low failure strains. However, the low failure strains of these stiff materials limit the stretchability of the reinforced synthetic biomaterials. By using the modified horseshoe lattice structure proposed in this paper, the failure strain mismatch between the stiff reinforcing materials and the soft matrix is resolved. Compared to other 3D printed tissue scaffolds that generally have small stretchability,[51–53] the current design can stretch up to 100%, and thus can match the stretchability of the soft matrix. Moreover, all of the modulus, stretchability and Poisson ratio can be tuned by varying the geometrical parameters L, R, w and θ_0.

Fig. 13 shows the design space of the rectangular horseshoe lattice structures under uniaxial tensile loading by using the theoretical framework. The design space is explored by varying the geometrical parameters w and L, under the following constraints: the maximum of the local strain ε_l of the lattice structure is smaller than a critical failure strain ε_f. w is set as w = 1.5, 2, 3, 4, 6, 8, 10, 12 or 14 × w_0, and L = 0, 2, 4, or 6 × w_0, where w_0 = 0.133 mm. w cannot be too small, or the lattice structure is too thin to be 3D printed. L and w also cannot be too large, otherwise the straight beam will overlay with the arc regions. Other parameters are fixed as: R = 1.33 mm, d = 1 mm, $\theta_0 = \pi/2$ and E = 1.2 GPa. The local strain of the beams consists of the elongation and the bending strain: $\varepsilon_l = \varepsilon + \kappa z$, $(-w/2 < z < w/2)$,

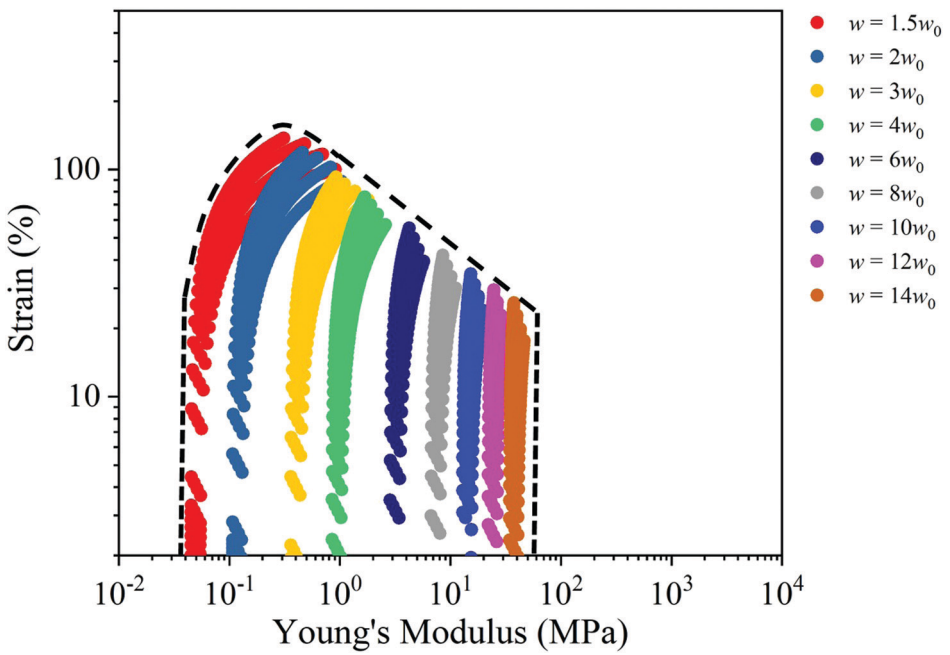

Fig. 13 Design space of the rectangular lattice structure.

where $\varepsilon = N/EA$ is the strain of the centerline of the lattice structure and $\kappa = M/EI$ is the local curvature. The critical failure strain is set as 10%. It should be noted that the average failure strain of the Vero material is generally larger than 20%.[54] Thus, the failure strain of 10% is chosen to make sure the lattice structure is reliable. Each point in Fig. 13 represents the corresponding tensile strain and the Young's modulus of the lattice structure. The design space is then roughly plotted using a dashed curve that covers all the points. The same design space is plotted on Fig. 1. It can be seen that the design space provided by the lattice structure can match the Young's modulus and stretchability of most of the soft materials.

It should also be noted that there is a turning point of the stress–strain curve of the rectangular lattice structure using the theoretical model, as shown in Fig. S1 in the ESI.† After the stress reaches a critical value σ_c, the theoretical model predicts that the periodical unit will tend to rotate to resist the increasing stress. The strain will decrease instead with increasing stress. However, the experiments were conducted under a strain control mode and exceeding rotation of the unit is limited due to the constraints on the transverse direction. Thus, a large discrepancy exists between experiments and theoretical modeling after $\sigma > \sigma_c$. This behavior has not been observed for the triangular lattice structure.

In our theoretical model, linear elasticity is assumed for the material. Viscosity and plasticity are neglected. However, Vero is a polymer with large viscosity. In order to reduce the effect of its viscosity, a slow loading rate is used in the experiments. As the strain is large, plastic deformation exists for the lattice structure, which also contributes a lot to the discrepancy between the theoretical and experimental results.

The current design of the lattice structure is intrinsically 2D and cannot be stretched along the thickness direction. In order to provide better performance, a 3D lattice structure can be designed by connecting the current design layer by layer with horseshoe microstructures. In this way, the lattice structures can be stretched along the thickness direction.

Another concern is the interfacial bonding between the reinforced lattice and the hydrogel. From our experimental results, we found that the fabricated hydrogels with 3D printed lattice structures break in the hydrogel region rather than at the interface after being stretched, suggesting that the interface between the hydrogel and the lattice structures is reasonably tough.[49] So, we believe that water molecules do not decrease the bonding strength between the reinforcement lattice and hydrogel matrix. We attribute the strong interfacial bonding to covalent bonds between the hydrogels and VeroCyan (Fig. S2 in ESI†). The surface of the printed lattice structures still has unreacted acrylate-based monomers, which covalently bond with the unreacted double bonds on acrylamide or PEGDA in the hydrogel precursor upon UV irradiation.

6 Conclusions

This study uses the concept of embedding stretchable rectangular/triangular lattice scaffolds into a soft elastic matrix as a means of creating synthetic composites that exhibit tunable mechanical and geometrical properties. A theoretical framework is developed to model the mechanical behaviors of the lattice scaffold and validated by both experimental results and finite element simulation. The validated theory is then used to predict the elastic performance of the lattice scaffold and guide the design of lattice scaffold-reinforced hydrogels. The results show that by rational design of the lattice scaffolds, tunable elastic moduli (a few kPa to hundreds of MPa), high stretchabilities (strain up to 180%) and a wide range of Poisson ratios (ranging from −0.5 to 1.2) can be obtained. By embedding the lattice into a soft matrix, a wide range of design space could be achieved for the biomaterial composites. This work could aid the design of soft biomaterials and have potential applications in tissue engineering, drug delivery and intraocular lenses.

Conflicts of interest

There are no conflicts to declare.

Acknowledgements

D. W. acknowledges the support by grants from the National Natural Science Foundation of China (Grant No. 51905336), the Shanghai Sailing Program (19YF1423000) and Digital Manufacturing and Design Centre at SUTD. Q. G. acknowledges the support by the Centers for Mechanical Engineering Research and Education at MIT and SUSTech. B. Z. acknowledges the support by Fundamental Research Funds for the Central Universities (no. 31020190QD015) and the National Natural Science Foundation of China (no. 51903210).

Notes and references

1 F. J. O'brien, *Mater. Today*, 2011, **14**, 88–95.
2 M. Lutolf and J. Hubbell, *Nat. Biotechnol.*, 2005, **23**, 47.
3 B. D. Ratner, A. S. Hoffman, F. J. Schoen and J. E. Lemons, *MRS Bull.*, 2006, **31**, 59.
4 M. Kanamala, W. R. Wilson, M. Yang, B. D. Palmer and Z. Wu, *Biomaterials*, 2016, **85**, 152–167.
5 R. Langer and N. A. Peppas, *AIChE J.*, 2003, **49**, 2990–3006.
6 A. Hasan, A. Memic, N. Annabi, M. Hossain, A. Paul, M. R. Dokmeci, F. Dehghani and A. Khademhosseini, *Acta Biomater.*, 2014, **10**, 11–25.
7 L. Xue and H. P. Greisler, *J. Vasc. Surg.*, 2003, **37**, 472–480.
8 J. Nguyen and L. Werner, Webvision: The Organization of the Retina and Visual System [Internet], University of Utah Health Sciences Center, 2017.
9 G. S. Karanasiou, M. I. Papafaklis, C. Conway, L. K. Michalis, R. Tzafriri, E. R. Edelman and D. I. Fotiadis, *Ann. Biomed. Eng.*, 2017, **45**, 853–872.
10 D. Bezuidenhout, D. F. Williams and P. Zilla, *Biomaterials*, 2015, **36**, 6–25.
11 H.-J. Kim, K. Zhang, L. Moore and D. Ho, *ACS Nano*, 2014, **8**, 2998–3005.

12 A. Lopez-Rubio, R. Gavara and J. M. Lagaron, *Trends Food Sci. Technol.*, 2006, **17**, 567–575.
13 C. E. Caicedo-Carvajal, Q. Liu, Y. Remache, A. Goy and K. S. Suh, *J. Tissue Eng.*, 2011, **2011**, 362326.
14 Y. Gong, L. He, J. Li, Q. Zhou, Z. Ma, C. Gao and J. Shen, *J. Biomed. Mater. Res., Part B*, 2007, **82**, 192–204.
15 M. S. Lopes, A. Jardini and R. Maciel Filho, *Procedia Eng.*, 2012, **42**, 1402–1413.
16 Z. Pan and J. Ding, *Interface Focus*, 2012, **2**, 366–377.
17 E. Pedraza, A.-C. Brady, C. A. Fraker and C. L. Stabler, *J. Biomater. Sci., Polym. Ed.*, 2013, **24**, 1041–1056.
18 Y. An and J. A. Hubbell, *J. Controlled Release*, 2000, **64**, 205–215.
19 H. Li, N. Davison, L. Moroni, F. Feng, J. Crist, E. Salter, C. O. Bingham and J. Elisseeff, *Cartilage*, 2012, **3**, 128–140.
20 I.-C. Liao, F. T. Moutos, B. T. Estes, X. Zhao and F. Guilak, *Adv. Funct. Mater.*, 2013, **23**, 5833–5839.
21 S. Lin, C. Cao, Q. Wang, M. Gonzalez, J. E. Dolbow and X. Zhao, *Soft Matter*, 2014, **10**, 7519–7527.
22 J.-Y. Sun, X. Zhao, W. R. Illeperuma, O. Chaudhuri, K. H. Oh, D. J. Mooney, J. J. Vlassak and Z. Suo, *Nature*, 2012, **489**, 133.
23 C. A. DeForest and K. S. Anseth, *Annu. Rev. Chem. Biomol. Eng.*, 2012, **3**, 421–444.
24 J. Malda, J. Visser, F. P. Melchels, T. Jüngst, W. E. Hennink, W. J. Dhert, J. Groll and D. W. Hutmacher, *Adv. Mater.*, 2013, **25**, 5011–5028.
25 A. Brunon, K. Bruyere-Garnier and M. Coret, *J. Biomech.*, 2010, **43**, 2221–2227.
26 F. T. Moutos, L. E. Freed and F. Guilak, *Nat. Mater.*, 2007, **6**, 162.
27 A. N. Annaidh, K. Bruyère, M. Destrade, M. D. Gilchrist and M. Otténio, *J. Mech. Behav. Biomed. Mater.*, 2012, **5**, 139–148.
28 A. Gallagher, A. N. Annaidh and K. Bruyère, *et al.*, IRCOBI Conference 2012, 12–14 September 2012, Dublin (Ireland), 2012.
29 K.-I. Jang, H. U. Chung, S. Xu, C. H. Lee, H. Luan, J. Jeong, H. Cheng, G.-T. Kim, S. Y. Han and J. W. Lee, *et al.*, *Nat. Commun.*, 2015, **6**, 6566.
30 G. H. Borschel, K. F. Kia, W. M. Kuzon Jr and R. G. Dennis, *J. Surg. Res.*, 2003, **114**, 133–139.
31 M. B. Christensen, K. Oberg and J. C. Wolchok, *SpringerPlus*, 2015, **4**, 142.
32 A. R. Kemper, A. C. Santago, J. D. Stitzel, J. L. Sparks and S. M. Duma, *J. Biomech.*, 2012, **45**, 348–355.
33 S. Umale, C. Deck, N. Bourdet, P. Dhumane, L. Soler, J. Marescaux and R. Willinger, *J. Mech. Behav. Biomed. Mater.*, 2013, **17**, 22–33.
34 P. Aguiari, M. Fiorese, L. Iop, G. Gerosa and A. Bagno, *Interact. Cardiovasc. Thorac. Surg.*, 2015, **22**, 72–84.
35 D. A. Morrow, T. L. H. Donahue, G. M. Odegard and K. R. Kaufman, *J. Mech. Behav. Biomed. Mater.*, 2010, **3**, 124–129.
36 J. Louis-Ugbo, B. Leeson and W. C. Hutton, *Clinical Anatomy*, 2004, **17**, 30–35.
37 C. Maganaris and M. Narici, in *Mechanical properties of tendons. Tendon injuries-basic science and clinical medicine*, ed. N. Maffulli, P. Renstrom and W. B. Leadbetter, 2005.
38 V. I. Egorov, I. V. Schastlivtsev, E. V. Prut, A. O. Baranov and R. A. Turusov, *J. Biomech.*, 2002, **35**, 1417–1425.
39 M. Zens, M. J. Feucht, J. Ruhhammer, A. Bernstein, H. O. Mayr, N. P. Südkamp, P. Woias and P. Niemeyer, *J. Exp. Orthop.*, 2015, **2**, 7.
40 J. R. Wünsch, *Polystyrene: Synthesis, production and applications*, iSmithers Rapra Publishing, 2000, vol. 112.
41 Q. T. Nguyen, Y. Hwang, A. C. Chen, S. Varghese and R. L. Sah, *Biomaterials*, 2012, **33**, 6682–6690.
42 J.-S. Yoon, S.-H. Oh, M.-N. Kim, I.-J. Chin and Y.-H. Kim, *Polymer*, 1999, **40**, 2303–2312.
43 N. Naik, J. Caves, E. L. Chaikof and M. G. Allen, *Adv. Healthcare Mater.*, 2014, **3**, 367–374.
44 Y. Hong, A. Huber, K. Takanari, N. J. Amoroso, R. Hashizume, S. F. Badylak and W. R. Wagner, *Biomaterials*, 2011, **32**, 3387–3394.
45 Q. Ma, H. Cheng, K.-I. Jang, H. Luan, K.-C. Hwang, J. A. Rogers, Y. Huang and Y. Zhang, *J. Mech. Phys. Solids*, 2016, **90**, 179–202.
46 L. H. Timmins, Q. Wu, A. T. Yeh, J. E. Moore Jr and S. E. Greenwald, *Am. J. Physiol.*, 2010, **298**, H1537–H1545.
47 R. Lakes, *Nature*, 2001, **414**, 503.
48 L. Landau, E. Lifshitz and J. Sykes, *Theory of Elasticity*, Pergamon Press, 1989.
49 B. Zhang, S. Li, H. Hingorani, A. Serjouei, L. Larush, A. A. Pawar, W. H. Goh, A. H. Sakhaei, M. Hashimoto, K. Kowsari, S. Magdassi and Q. Ge, *J. Mater. Chem. B*, 2018, **6**, 3246–3253.
50 A. A. Pawar, G. Saada, I. Cooperstein, L. Larush, J. A. Jackman, S. R. Tabaei, N.-J. Cho and S. Magdassi, *Sci. Adv.*, 2016, **2**, e1501381.
51 M. Al Rifaie, A. Mian and R. Srinivasan, *Proc. Inst. Mech. Eng., Part L*, 2019, **233**, 1574–1584.
52 P. F. Egan, V. C. Gonella, M. Engensperger, S. J. Ferguson and K. Shea, *PLoS One*, 2017, **12**, e0182902.
53 P. F. Egan, K. A. Shea and S. J. Ferguson, *Biomech. Model. Mechanobiol.*, 2018, **17**, 1481–1495.
54 S. Akbari, A. H. Sakhaei, K. Kowsari, B. Yang, A. Serjouei, Z. Yuanfang and Q. Ge, *Smart Mater. Struct.*, 2018, **27**, 065027.

